

Solution ✓ Cite This: ACS Energy Lett. 2020, 5, 17–22

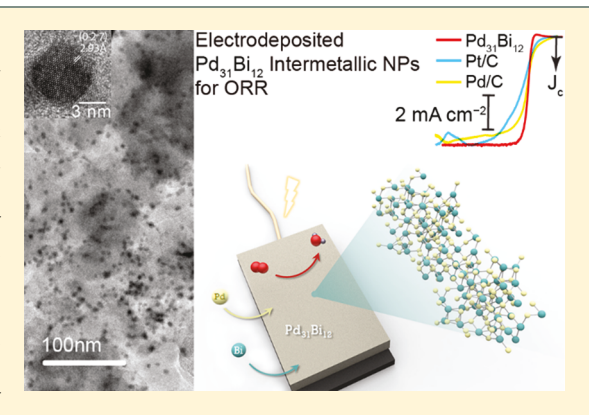
Pulsed Electrodeposition of Metastable Pd₃₁Bi₁₂ Nanoparticles for Oxygen Reduction Electrocatalysis

Yunfei Wang and Anthony Shoji Hall*®

Department of Materials Science and Engineering, Johns Hopkins University, Baltimore, Maryland 21218, United States

Supporting Information

ABSTRACT: Metastable alloys have recently emerged as highperformance catalysts, extending the toolbox of binary alloy materials that can be utilized to mediate electrocatalytic reactions. In particular, nanostructured metastable ordered intermetallic compounds are challenging to synthesize. Here we report a method for synthesizing sub-15 nm metastable ordered intermetallic Pd₃₁Bi₁₂ nanoparticles at room temperature, in a single step, by pulsed electrochemical deposition onto high surface area carbon supports. The resulting Pd31Bi12 nanoparticles displays a 7× enhancement of the mass activity relative to Pt/C and a 4× enhancement relative to Pd/C for the oxygen reduction reaction (ORR). The high performance of Pd₃₁Bi₁₂ nanoparticles is demonstrated to arise from reduced oxygen binding caused by alloying of Pd with Bi. We also demonstrate that the isolation of Pd sites from each other facilitates methanol-tolerant ORR behavior.



etastable materials offer the opportunity to explore new materials for electrocatalysis beyond conventional equilibrium phases. 1-9 Metastable ordered intermetallic compounds offer unparalleled control of material properties by providing uniform local atomic structure from long range atomic ordering, and by allowing one to access various structural variations of materials with the same composition.^{3,5,10} However, synthetic methods for manipulating the nanoscale morphology of metastable ordered intermetallic compounds is difficult because principles that govern their formation are poorly understood. 3,5,11,12 Catalyst activity and selectivity are impacted by the atomic structure and morphology of the electrode. The lack of morphological control of metastable ordered intermetallic materials is hampering its progress for advancing the field of electrocatalysis.

Nanostructured metastable ordered intermetallic compounds are difficult to rationally synthesize because the nucleation and growth conditions required to access these phases are not unequivocally known.^{23–27} Literature reports suggest that the formation of metastable ordered intermetallic nanoparticles can occur only under conditions in which interfacial stabilization by capping agents results in greater stability for the metastable phase relative to equilibrium phases or under conditions in which nucleation rather than solid-state diffusion is rate-limiting. 5,11,28-30 However, the former case is difficult to predict from first-principles, while the latter often

results in materials with poor atomic ordering.^{4,5,31,32} Hence, conventional synthetic methods, such as high-temperature annealing and/or colloidal synthesis, largely exclude the formation of metastable ordered intermetallic compounds under typical reaction conditions.^{31,33–35} Electrochemical deposition has recently emerged as a flexible technique for the direct preparation of metastable alloys and ordered intermetallic phases, yielding materials which can possess high intrinsic catalytic performance. ^{2,3,36} However, these techniques are limited to the preparation of thin films on flat/nonporous substrates, precluding their implementation in application-relevant contexts that require high surface area, and for designing materials that can harness diffusional transport gradients for enhancing catalytic activity and/or selectivity. 13,14

To overcome this shortcoming, we herein describe a method utilizing pulsed electrochemical deposition to decouple nucleation from growth kinetics, allowing for the direct synthesis of sub-15 nm diameter metastable ordered intermetallic Pd31Bi12 nanoparticles that uniformly decorate commercial carbon black supports. Thermodynamic phase diagrams indicated that Pd₃₁Bi₁₂ is stable above 500 °C; remarkably, we are able to access this material under conditions in which it is not predicted to be thermodynami-

Received: October 10, 2019 Accepted: November 17, 2019 Published: November 25, 2019



cally stable.³⁷ Pulsed electrochemical deposition allows us to access a nonequilibrium synthetic environment, promoting the synthesis of metastable ordered intermetallic nanoparticles.³⁶ The resulting $Pd_{31}Bi_{12}$ nanoparticles achieve a surface area of $\sim 37~m^2/g_{pd}$, which is nearly 40× higher than that of conventional electrodeposition processes that yield low-porosity thin film morphologies.³ To the best of our knowledge, this is the first report of metastable ordered intermetallic nanoparticles dispersed onto carbon supports prepared by electrochemical deposition at room temperature and atmospheric pressure. We demonstrate that finely dispersed $Pd_{31}Bi_{12}$ nanoparticles on carbon supports exhibit high mass activities for the oxygen reduction reaction (ORR) and methanol-tolerant oxygen reduction electrocatalysis.

To achieve isolated nanoparticles of metastable Pd₃₁Bi₁₂, we used high surface area carbon, Vulcan XC-72 (The Fuel Cell Store), as the support. We utilized a pulsed potentiostatic waveform at a large overpotential to initiate nucleation uniformly over the surface of the high surface area carbon, followed by constant-potential deposition to grow the deposited nuclei (Figure 1). To identify the crystal structure

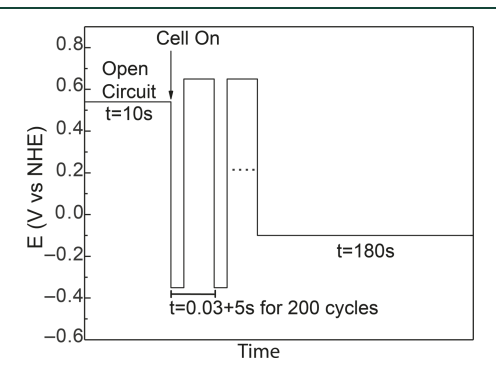


Figure 1. Potentiostatic waveform used to deposit $Pd_{31}Bi_{12}$. The open-circuit potential is typically \sim 0.54 V. Voltages are shown vs the NHF

of the as-deposited sample, powder X-ray diffraction (XRD) patterns were obtained by scratching off the film onto doublesided kapton tape (Figure 2a). The primary peaks obtained in the diffractogram match the simulated Pd31Bi12 pattern, indicating that phase-pure Pd₃₁Bi₁₂ was formed.³⁷ The primary reflections of the deposited Pd31Bi12 are broad; Scherrer analysis of the (1 1 15) reflection indicates that the average grain size of the Pd₃₁Bi₁₂ is ~15 nm (Figure 2b). Images collected by transmission electron microscopy (TEM) indicated that Pd31Bi12 was dispersed uniformly on carbon with an average particle size of ~13 nm, which agrees with the value estimated by the Scherrer analysis (Figure 2b-d). Highresolution TEM images of Pd31Bi12 indicate the particles are single-crystalline, with an observed lattice spacing of ~2.93 Å, which can be indexed to the (0 2 7) plane. The rings from the selected area electron diffraction (SAED) image from the same region in Figure 2c can be indexed to the (1 1 15), (1 1 18), (3 3 0), (2 2 18), and (5 3 18) reflections of Pd₃₁Bi₁₂. Remarkably, we can access nanoparticles of this material at room temperature in minutes, while the preparation of metastable stable phases by other methods is not straightforward.

We explored the electrochemical performance of the $Pd_{31}Bi_{12}$ supported on carbon, henceforth denoted as $Pd_{31}Bi_{12}/C$, for ORR and compared it to commercial Pd/C

(Premetek) and Pt/C (TKK). The ORR performance was assessed by collecting linear sweep voltammograms (LSVs) of Pd₃₁Bi₁₂/C, Pd/C, and Pt/C with the material supported on a glassy carbon rotating disk electrode (Figure 3a). The current onset for ORR on Pd₃₁Bi₁₂/C (0.97 V) is more negative than that of Pt/C (1.03 V) and Pd/C (1.09 V). However, the current density of Pd₃₁Bi₁₂ increases faster than that of Pt/C and Pd/C with increasing overpotential, resulting in a greater current density below 0.94 V. The half-wave potential $(E_{1/2})$ of $Pd_{31}Bi_{12}/C$ is 0.92 V, whereas Pt/C and Pd/C display $E_{1/2}$ values of 0.87 and 0.91 V, respectively. At 0.90 V, the specific and mass activities of $Pd_{31}Bi_{12}/C$ (2.42 \pm 0.20 mA/cm²_{Pd}, 0.95 \pm 0.18 A/mg_{Pd}) are larger than those of Pt/C (0.32 \pm 0.20 mA/cm_{Pt}^2 0.13 \pm 0.04 A/mg_{Pt}) and Pd/C (0.62 \pm 0.04 mA/ cm^2_{Pd} , 0.20 \pm 0.02 A/mg_{Pd}). The activities of electrodeposited Pt/C and Pd/C were also measured and found to be comparable to those of commercial Pt/C and Pd/C samples (Figure S1). The \sim 4-fold enhancement of activity compared to that of Pd/C and ~7-fold enhancement of activity relative to that of Pt/C indicate that Pd₃₁Bi₁₂/C exhibits excellent performance for ORR.

Accelerated durability testing (ADT) was utilized to determine the stability of the materials by cycling the voltage repeatedly between 0.6 and 1.0 V at a sweep rate of 100 mV/s scan, simulating long-term fuel cell operation. The specific and mass activities of Pd₃₁Bi₁₂/C decrease from 2.42 to 1.35 mA/ cm²_{Pd} and 0.95 to 0.54 A/mg_{Pd} after 10k cycles, indicating a retention of ~60% of the initial activity (Figure 3b). The activity retention for Pt/C was ~70% for both the mass and specific activity, which is comparable to those of Pd₃₁Bi₁₂/C. However, the activity retention of Pd/C was ~30%, which indicates that it is less stable than Pd₃₁Bi₁₂/C. The specific surface areas for all samples decrease by 10-15% after ADT, indicating that the loss of activity is probably caused by some particle aggregation from migration and coalescence or by corrosion and redeposition, and by elimination of highly active sites via surface reconstructions (Figure 3c).³⁸ The stability of electrodeposited Pd/C and Pt/C samples was comparable to that of commercial Pt/C and Pd/C samples, indicating that electrodeposition does not enhance the intrinsic interaction of the material with the carbon support (Figures S1 and S2). High-resolution TEM and electron diffraction after ADT indicates that the intermetallic crystallinity of Pd₃₁Bi₁₂/C is retained (Figure S3). The enhanced stability of Pd₃₁Bi₁₂/C relative to that of Pd/C may be caused by higher corrosion resistance and/or by enhanced affinity of Pd31Bi12 with the carbon support.

To understand why $Pd_{31}Bi_{12}/C$ is more active than elemental Pd/C, we measured CVs of both samples in N_2 -saturated 0.1 M KOH (Figure 3d). We observed that $Pd_{31}Bi_{12}/C$ does not exhibit hydrogen underpotential deposition (H-UPD), in stark contrast to Pd/C, which exhibits clear H-UPD waves from ~ 0 to ~ 0.4 V. The surface oxidation and reduction feature of $Pd_{31}Bi_{12}/C$, which occurs above 0.6 V, displays a sharper feature relative to Pd/C. In addition to this, the Pd oxide reduction peak of $Pd_{31}Bi_{12}/C$ (0.750 V) shifts by 31 mV toward more positive potentials relative to Pd/C (0.719 V), indicating that the Pd-O bond has substantially weakened. Pd adsorbs oxygen-based intermediates too strongly; hence, lowering the Pd-O bond energy can enhance catalysis as indicated by the Sabatier principle. 7,15,18,39

Low-temperature fuel cells can utilize small molecules, such as methanol, for the anode reaction. Alkaline membranes are

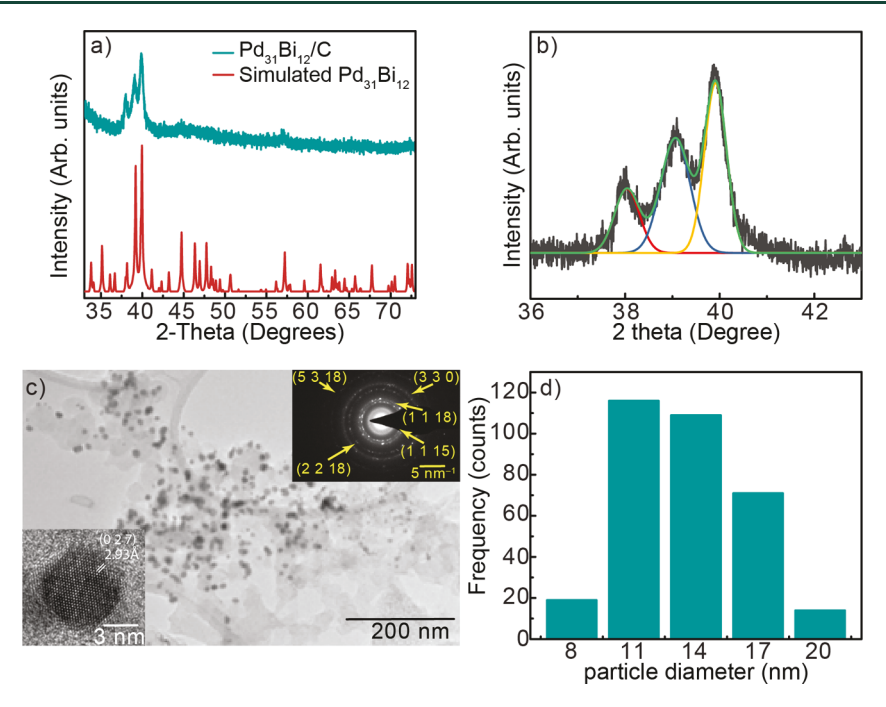


Figure 2. (a) X-ray diffraction pattern of electrodeposited $Pd_{31}Bi_{12}/C$, (b) zoom-in of the three primary reflections that are peak-fitted. The Scherrer equation was used to determine the grain size from the fitted peak at the (1 1 15) plane at 39°. The simulated $Pd_{31}Bi_{12}$ diffraction patterns are from ICSD collection code 616947. (c) Representative TEM image of $Pd_{31}Bi_{12}/C$ nanoparticles and corresponding SAED pattern. (d) Particle size histogram of $Pd_{31}Bi_{12}/C$; the average particle size is 13 nm.

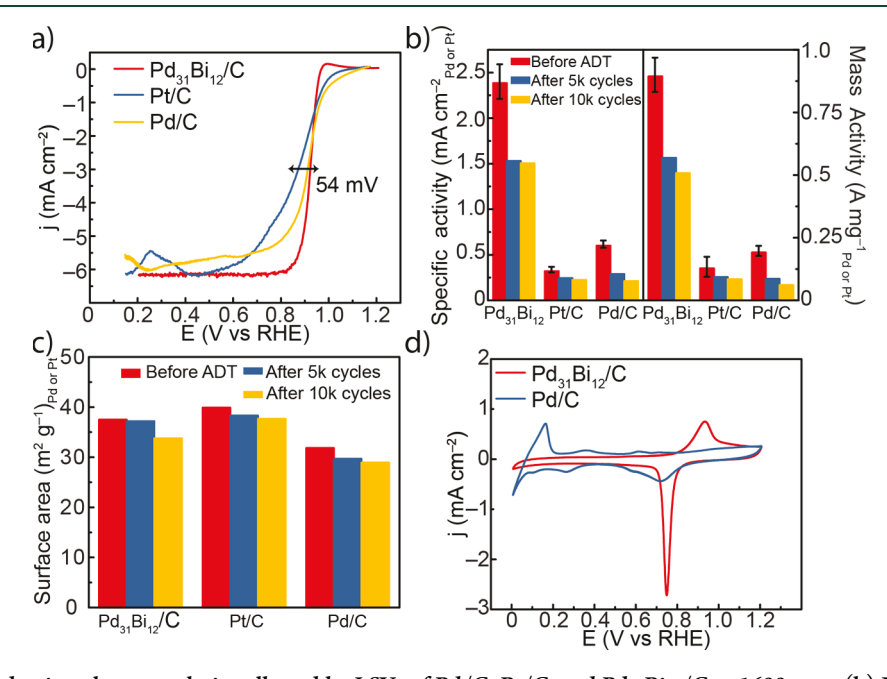


Figure 3. (a) Oxygen reduction electrocatalysis collected by LSVs of Pd/C, Pt/C, and Pd $_{31}$ Bi $_{12}$ /C at 1600 rpm. (b) Mass transport corrected specific activity at 0.90 V vs RHE for fresh samples and samples subjected to 5k and 10k cycles of ADT. (c) Specific surface areas for fresh and samples subjected to 5k and 10k cycles of ADT. (d) CV of Pd $_{31}$ Bi $_{12}$ /C and Pd/C in N $_{2}$ -saturated 0.1 M KOH collected at a sweep rate of 20 mV/s. All ORR measurements were performed in O $_{2}$ -saturated 0.1 KOH electrolyte with a catalyst loading of \sim 24 μ g/cm 2 on a precious metal basis.

permeable to methanol, which allows significant crossover from the anode to the cathode during fuel cell operation. Pt and Pd are excellent catalysts for the electrooxidation of methanol; however, this reaction occurs in the same potential range as ORR, decreasing the efficiency of Pt and Pd for performing ORR. Recent studies have shown that multiple neighboring Pt or Pd metal sites (large site ensembles) are

required for methanol oxidation to occur; however, large site ensembles are not required for ORR. The atomic ordering of the atoms in ordered intermetallic $Pd_{31}Bi_{12}$ maximizes the number of bonds between Pd and Bi and minimize the number of possible Pd–Pd bonds, resulting in small ensembles of Pd sites. Inspection of the $Pd_{31}Bi_{12}$ crystal structure indicates that the number of Pd–Pd bonds present on the surface is <5 for

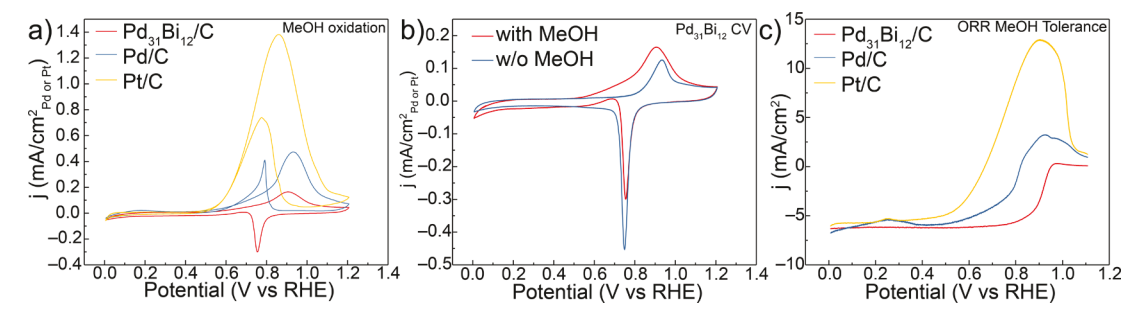


Figure 4. (a) Methanol oxidation on $Pd_{31}Bi_{12}/C$, Pd/C, and Pt/C collected in N_2 -saturated 0.1 M KOH with 0.5 M methanol. (b) CV of $Pd_{31}Bi_{12}/C$ in N_2 -saturated 0.1 M KOH with and without methanol. (c) ORR on $Pd_{31}Bi_{12}/C$, Pd/C, and Pt/C in N_2 -saturated 0.1 M KOH with 0.5 M methanol. All samples were measured at 1600 rpm on a rotating disk electrode with a scan rate of 20 mV/s.

the low index facets, indicating that Pd31Bi12 should be a poor catalyst for methanol oxidation because of small Pd ensembles. To test this hypothesis, we measured the oxidation of methanol on N2-saturated 0.1 M KOH with 0.5 M methanol (Figure 4a) on Pd/C, Pt/C, and Pd₃₁Bi₁₂/C. The oxidation of methanol can be clearly seen in Pt/C and Pd/C as two characteristic oxidation peaks are observed in the forward and return scans at $\sim 0.9-0.95$ and at 0.77 V, respectively. In contrast, the CV of Pd₃₁Bi₁₂/C in methanol appears similar to CVs collected in methanol-free solution (Figure 4a,b). Pd₃₁Bi₁₂/C exhibits a small increase in the baseline current at voltages more positive than 0.5 V when methanol is present in the anodic scan direction; however, the peak potential of the anodic wave (~0.9 V) overlays with the wave collected in a methanol-free solution (Figure 4b). In the return scan, the Pd oxide reduction peak overlays with that of methanol-free solutions, showing a small anodic increase in the current between 0.6 and ~0.7 V. Nevertheless, Pd₃₁Bi₁₂/C reacts poorly with methanol, indicating that it should exhibit high methanol tolerance during ORR. To assess the ORR methanol tolerance, we performed ORR electrocatalysis in the presence of 0.5 M methanol (Figure 4c). The voltammograms indicate that ORR was completely suppressed at voltages more positive than 0.6 V for Pt/C and Pd/C from methanol oxidation, as indicated by the large oxidative wave. The ORR can outcompete methanol oxidation at voltages more negative than 0.6 V, increasing the overpotential for ORR by >200 mV on Pt/C and Pd/C. In contrast, a minor shift of 11 mV is observed for the half-wave potential of Pd₃₁Bi₁₂/C for ORR, indicating that the presence of methanol hardly interferes with its ORR activity. The minimization of surface Pd-Pd bonds afforded by atomic-scale ordering allows Pd₃₁Bi₁₂/C to possess superior methanol-tolerant ORR behavior.

In summary, we developed a method to prepare nanoparticles of metastable ordered intermetallic compounds at room temperature with a simple method. By decoupling nucleation from growth steps, we were able to uniformly decorate carbon black supports with $\mathrm{Pd}_{31}\mathrm{Bi}_{12}$ nanocrystals. The $\mathrm{Pd}_{31}\mathrm{Bi}_{12}/\mathrm{C}$ exhibits superior electrocatalytic performance for ORR and excellent methanol-tolerance relative to Pd/C and Pt/C . We believe that this technique can be extended to synthesize other metastable ordered intermetallic compounds directly on high surface area supports at room temperature.

EXPERIMENTAL METHODS

Materials. Palladium(II) nitrate hydrate (99.9% metals basis, Alfa Aesar), sodium tetrachloroplatinate(II) hydrate (Premion, 99.95% metals basis, Alfa Aesar), bismuth(III) acetate

(Bi(Oac)₃, 99.99%, Alfa Aesar), 40% Pd on Vulcan XC-72 (Premetek Co), O_2 gas (UHP grade, Airgas), and 40% Pt on high surface area carbon (TEC10E40E, Tanaka Kikinzoku Kogyo TKK) were used as received without purification. Electrolyte solutions were prepared with deionized water (resistance: 18.2 M Ω) and potassium hydroxide (KOH, semiconductor-grade 99.99%, Alfa Aesar).

Physicochemical Characterization. The nanoparticles were drop-casted onto a zero-background Si wafer and examined with a Philips X'Pert Pro powder X-ray diffractometer (XRD) with CuK radiation ($K\alpha_1$, $\lambda=1.5406$ Å and $K\alpha_2$, $\lambda=1.5444$ Å). TEM was performed on an FEI F200C Talos or FEI Tecnai TF30 operated at 200 kV. The materials supported on the glassy carbon disk after electrochemical testing were dissolved with concentrated nitric acid and then diluted with water. The metal concentration in the nitric acid solution was analyzed by the PerkinElmer NexION 300D with ICP.

Oxygen Reduction Measurements. Electrochemical measurements were carried out with a potentiostat/galvanostat (Metrohm Autolab potentiostat or Nuvant EzStat Pro) in a three-electrode cell made from Teflon. KOH solutions (0.1 M) were used as the electrolyte for all experiments. A Hg/HgO electrode filled with 1 M NaOH was used as the reference electrode. A graphite rod was used as the counter electrode. The Hg/HgO reference electrode potential was periodically checked versus a reversible hydrogen electrode (RHE) to verify the stability of the reference potential. The potential vs the NHE was determined from the following equation: $E(NHE) = E_{applied}(Hg/HgSO_4) + 0.14 \text{ V}$. The potential vs the RHE was determined with the following equation: E(RHE) = E(NHE) + 0.059pH. ORR testing was performed by sweeping the voltage from -0.9 to 0.3 V vs Hg/HgO at a sweep rate of 20 mV/s. All measurements were performed on a 5 mm diameter glassy carbon disk electrode that was rotated at 1600 rpm. All ORR measurements were IR-corrected, and the IR drop was measured by the positive feedback or current interrupt method.

Mass transport correction to obtain the kinetic current density was obtained via the Koutecky–Levich Method.⁴¹ The following expression was used

$$J_{k} = \frac{J_{\lim} \times J}{J_{\lim} - J}$$

where $J_{\rm lim}$ is the limiting current density, $J_{\rm k}$ is the kinetic current density, and J is the current density at a given voltage. Electrochemical Methanol Oxidation and Methanol-Tolerant ORR Measurements. Methanol oxidation was measured by cycling the voltage from -0.9 to 0.3 V vs Hg/HgO at a sweep

rate of 20 mV/s in a solution containing N_2 -saturated 0.1 M KOH + 0.5 M MeOH at 1600 rpm. Methanol-tolerant ORR measurements were carried out by cycling the voltage from -0.9 to 0.3 V vs Hg/HgO at a sweep rate of 20 mV/s in a solution containing O_2 -saturated 0.1 M KOH + 0.5 M MeOH while the electrode was rotated at 1600 rpm.

Preparation of Commercial Pt/C and Pd/C Electrodes. To prepare Pd/C materials, 30 mg of 40% Pd on Vulcan XC-72 (Premetek Co) was dispersed into a solution consisting of a mixture of 8 μ L of Nafion ionomer, 1 mL of DI water, and 1 mL of IPA. The resulting solution was sonicated for 20 min. The mixture was drop-casted onto the 5 mm diameter disk to obtain a mass loading of ~24 μ g/cm². The Pt/C sample was prepared with the same procedure except with Pt/C (TKK) used in place of Pd/C.

Preparation of Pd31Bi12 Nanoparticles. Vulcan XC-72 was suspended in IPA and water (1:1 mixture by volume) by sonication and then drop-casted on the glassy carbon electrode with a loading of ~0.38 mg/cm². Pd₃₁Bi₁₂ ordered intermetallics were grown directly onto the carbon particles by deposition from an aqueous electrolyte containing 50 mM ethylenediammenetetracetic acid (EDTA), 25 mM Bi- $(C_2H_3O_2)_3$, and 4 mM Pd(NO₃)₂ at 30 °C. The pulse-on potential was chosen to be -0.35 V vs NHE, which is higher than the minimum potential to deposit Pd or Pd-Bi alloy; this was chosen to supply the necessary overpotential for fast nucleation. The pulse-on time was 30 ms so as to promote nucleation over particle growth. The pulse-reverse was chosen at 0.65 V vs NHE for 5 s to allow the local Pd cation concentration to relax to equilibrium, providing a uniform concentration profile during the on pulse, thereby decreasing the spatial variations of the potential distribution. 42 After 200 pulse cycles, chronoamperometry at −0.1 V was applied for 180 s to grow the deposited nuclei into ordered intermetallic $Pd_{31}Bi_{12}/C$; during this step, a current density of around -0.5mA/cm² was observed. The as-deposited sample was cleaned to remove organic residue, as described in our previous article.³

Preparation of Electrodeposited Pt/C and Pd/C Electrodes. Electrodeposited Pd/C and Pt/C were prepared with the same method as $Pd_{31}Bi_{12}$, except only 4 mM $Pd(NO_3)_2$ and 4 mM Na_2PtCl_4 were used as the metal sources, respectively.

Sample Preparation for ICP-MS Analysis. After electrochemical catalysis, the glassy carbon electrode was taken out of the electrolyte and rinsed with 18.2 M Ω water, dried in air, and placed in a plastic tube and sonicated in 1 mL of TraceMetal-grade nitric acid. An additional 9 mL of 18.2 M Ω water was added to the tube before the ICPMS measurement.

CO Stripping Measurements. CO stripping was used to determine the electrochemically active surface area (ECSA) of Pt or Pd atoms on the surface of the electrode. The electrodes were first held at 0.15 V vs RHE for 20 min in 0.1 M KOH saturated with CO to form a surface-adsorbed CO monolayer. The CO(aq) was removed by saturating the electrolyte with Ar or N₂ for 15 min. Finally, the voltage was swept from 0.15 to 1.15 V vs RHE to oxidize the surface-adsorbed CO layer. The surface area of the sample can be calculated by integrating the oxidation peak of the CO monolayer, assuming one CO adsorbed per Pd or Pt atom on the surface. The ratio of charge transferred for CO oxidation and metal surface area was estimated as 484 μ C/cm2 for Pt and 420 μ C/cm2 for Pd and Pd₃₁Bi₁₂.

ASSOCIATED CONTENT

S Supporting Information

The Supporting Information is available free of charge at https://pubs.acs.org/doi/10.1021/acsenergylett.9b02219.

Representative TEM images of $Pd_{31}Bi_{12}$ nanoparticles, mass transport corrected specific activity and mass activity of Pt/C and Pd/C, specific surface areas for electrodeposited Pd/C and Pt/C, and high-resolution TEM image of $Pd_{31}Bi_{12}$ and its resulting electron diffraction pattern after ADT (PDF)

AUTHOR INFORMATION

Corresponding Author

*E-mail: Shoji@jhu.edu.

ORCID ®

Anthony Shoji Hall: 0000-0003-4134-4160

Notes

The authors declare no competing financial interest.

ACKNOWLEDGMENTS

A.S.H. acknowledges financial support from the National Science Foundation under Award No. CHE-1764310 and Johns Hopkins University Catalyst Award.

REFERENCES

- (1) Higgins, D.; Wette, M.; Gibbons, B. M.; Siahrostami, S.; Hahn, C.; Escudero-Escribano, M. a.; García-Melchor, M.; Ulissi, Z.; Davis, R. C.; Mehta, A.; Clemens, B. M.; Nørskov, J. K.; Jaramillo, T. F. Copper Silver Thin Films with Metastable Miscibility for Oxygen Reduction Electrocatalysis in Alkaline Electrolytes. *ACS Applied Energy Materials* **2018**, *1* (5), 1990–1999.
- (2) Hwang, S.-M.; Bonevich, J. E.; Kim, J. J.; Moffat, T. P. Electrodeposition of Pt100-xPbx Metastable Alloys and Intermetallics. J. Electrochem. Soc. 2011, 158 (6), D307-D316.
- (3) Wang, Y.; Sun, D.; Chowdhury, T.; Wagner, J. S.; Kempa, T. J.; Hall, A. S. Rapid Room-Temperature Synthesis of a Metastable Ordered Intermetallic Electrocatalyst. *J. Am. Chem. Soc.* **2019**, *141* (6), 2342–2347.
- (4) Piburn, G. W.; Li, H.; Kunal, P.; Henkelman, G.; Humphrey, S. M. Rapid Synthesis of Rhodium—Palladium Alloy Nanocatalysts. *ChemCatChem* **2018**, *10* (1), 329—333.
- (5) Parija, A.; Waetzig, G. R.; Andrews, J. L.; Banerjee, S. Traversing Energy Landscapes Away from Equilibrium: Strategies for Accessing and Utilizing Metastable Phase Space. *J. Phys. Chem. C* **2018**, *122* (45), 25709–25728.
- (6) Holewinski, A.; Idrobo, J.-C.; Linic, S. High-performance Ag—Co alloy catalysts for electrochemical oxygen reduction. *Nat. Chem.* **2014**, *6*, 828.
- (7) Li, H.; Luo, L.; Kunal, P.; Bonifacio, C. S.; Duan, Z.; Yang, J. C.; Humphrey, S. M.; Crooks, R. M.; Henkelman, G. Oxygen Reduction Reaction on Classically Immiscible Bimetallics: A Case Study of RhAu. J. Phys. Chem. C 2018, 122 (5), 2712–2716.
- (8) Kusada, K.; Kobayashi, H.; Ikeda, R.; Kubota, Y.; Takata, M.; Toh, S.; Yamamoto, T.; Matsumura, S.; Sumi, N.; Sato, K.; Nagaoka, K.; Kitagawa, H. Solid Solution Alloy Nanoparticles of Immiscible Pd and Ru Elements Neighboring on Rh: Changeover of the Thermodynamic Behavior for Hydrogen Storage and Enhanced CO-Oxidizing Ability. J. Am. Chem. Soc. 2014, 136 (5), 1864–1871.
- (9) Zhou, S.; Jackson, G. S.; Eichhorn, B. AuPt Alloy Nanoparticles for CO-Tolerant Hydrogen Activation: Architectural Effects in Au-Pt Bimetallic Nanocatalysts. *Adv. Funct. Mater.* **2007**, *17* (16), 3099–3104.
- (10) Ma, T.; Wang, S.; Chen, M.; Maligal-Ganesh, R. V.; Wang, L.-L.; Johnson, D. D.; Kramer, M. J.; Huang, W.; Zhou, L. Toward Phase

and Catalysis Control: Tracking the Formation of Intermetallic Nanoparticles at Atomic Scale. *Chem.* **2019**, *5* (5), 1235–1247.

- (11) Vasquez, Y.; Luo, Z.; Schaak, R. E. Low-Temperature Solution Synthesis of the Non-Equilibrium Ordered Intermetallic Compounds Au3Fe, Au3Co, and Au3Ni as Nanocrystals. *J. Am. Chem. Soc.* **2008**, 130 (36), 11866–11867.
- (12) Yan, Y.; Du, J. S.; Gilroy, K. D.; Yang, D.; Xia, Y.; Zhang, H. Intermetallic Nanocrystals: Syntheses and Catalytic Applications. *Adv. Mater.* **2017**, 29 (14), 1605997.
- (13) Hall, A. S.; Yoon, Y.; Wuttig, A.; Surendranath, Y. Mesostructure-Induced Selectivity in CO2 Reduction Catalysis. *J. Am. Chem. Soc.* **2015**, *137* (47), 14834–14837.
- (14) Yoon, Y.; Hall, A. S.; Surendranath, Y. Tuning of Silver Catalyst Mesostructure Promotes Selective Carbon Dioxide Conversion into Fuels. *Angew. Chem., Int. Ed.* **2016**, *55* (49), 15282–15286.
- (15) Stamenkovic, V. R.; Fowler, B.; Mun, B. S.; Wang, G.; Ross, P. N.; Lucas, C. A.; Marković, N. M. Improved Oxygen Reduction Activity on Pt₃Ni(111) via Increased Surface Site Availability. *Science* **2007**, *315* (5811), 493–497.
- (16) Hoang, T. T. H.; Verma, S.; Ma, S.; Fister, T. T.; Timoshenko, J.; Frenkel, A. I.; Kenis, P. J. A.; Gewirth, A. A. Nanoporous Copper—Silver Alloys by Additive-Controlled Electrodeposition for the Selective Electroreduction of CO2 to Ethylene and Ethanol. *J. Am. Chem. Soc.* **2018**, *140* (17), 5791–5797.
- (17) Bu, L.; Zhang, N.; Guo, S.; Zhang, X.; Li, J.; Yao, J.; Wu, T.; Lu, G.; Ma, J.-Y.; Su, D.; Huang, X. Biaxially strained PtPb/Pt core/shell nanoplate boosts oxygen reduction catalysis. *Science* **2016**, 354 (6318), 1410–1414.
- (18) Bu, L.; Shao, Q.; Pi, Y.; Yao, J.; Luo, M.; Lang, J.; Hwang, S.; Xin, H.; Huang, B.; Guo, J.; Su, D.; Guo, S.; Huang, X. Coupled s-p-d Exchange in Facet-Controlled Pd₃Pb Tripods Enhances Oxygen Reduction Catalysis. *Chem.* **2018**, *4* (2), 359–371.
- (19) Huang, X.; Tang, S.; Mu, X.; Dai, Y.; Chen, G.; Zhou, Z.; Ruan, F.; Yang, Z.; Zheng, N. Freestanding palladium nanosheets with plasmonic and catalytic properties. *Nat. Nanotechnol.* **2011**, *6*, 28.
- (20) Bu, L.; Ding, J.; Guo, S.; Zhang, X.; Su, D.; Zhu, X.; Yao, J.; Guo, J.; Lu, G.; Huang, X. A General Method for Multimetallic Platinum Alloy Nanowires as Highly Active and Stable Oxygen Reduction Catalysts. *Adv. Mater.* 2015, 27 (44), 7204–7212.
- (21) Bu, L.; Guo, S.; Zhang, X.; Shen, X.; Su, D.; Lu, G.; Zhu, X.; Yao, J.; Guo, J.; Huang, X. Surface engineering of hierarchical platinum-cobalt nanowires for efficient electrocatalysis. *Nat. Commun.* **2016**, *7*, 11850.
- (22) Mariano, R. G.; McKelvey, K.; White, H. S.; Kanan, M. W. Selective increase in CO₂ electroreduction activity at grain-boundary surface terminations. *Science* **2017**, 358 (6367), 1187–1192.
- (23) Wang, D.; Xin, H. L.; Hovden, R.; Wang, H.; Yu, Y.; Muller, D. A.; DiSalvo, F. J.; Abruna, H. D. Structurally ordered intermetallic platinum-cobalt core-shell nanoparticles with enhanced activity and stability as oxygen reduction electrocatalysts. *Nat. Mater.* **2013**, *12* (1), 81–7.
- (24) Maligal-Ganesh, R. V.; Xiao, C.; Goh, T. W.; Wang, L.-L.; Gustafson, J.; Pei, Y.; Qi, Z.; Johnson, D. D.; Zhang, S.; Tao, F.; Huang, W. A Ship-in-a-Bottle Strategy To Synthesize Encapsulated Intermetallic Nanoparticle Catalysts: Exemplified for Furfural Hydrogenation. ACS Catal. 2016, 6 (3), 1754–1763.
- (25) Chen, H.; Wang, D.; Yu, Y.; Newton, K. A.; Muller, D. A.; Abruña, H.; DiSalvo, F. J. A Surfactant-Free Strategy for Synthesizing and Processing Intermetallic Platinum-Based Nanoparticle Catalysts. *J. Am. Chem. Soc.* **2012**, *134* (44), 18453–18459.
- (26) Ji, X.; Lee, K. T.; Holden, R.; Zhang, L.; Zhang, J.; Botton, G. A.; Couillard, M.; Nazar, L. F. Nanocrystalline intermetallics on mesoporous carbon for direct formic acid fuel cell anodes. *Nat. Chem.* 2010. 2, 286.
- (27) Xiong, Y.; Yang, Y.; Joress, H.; Padgett, E.; Gupta, U.; Yarlagadda, V.; Agyeman-Budu, D. N.; Huang, X.; Moylan, T. E.; Zeng, R.; Kongkanand, A.; Escobedo, F. A.; Brock, J. D.; DiSalvo, F. J.; Muller, D. A.; Abruña, H. D. Revealing the atomic ordering of

binary intermetallics using in situ heating techniques at multilength scales. *Proc. Natl. Acad. Sci. U. S. A.* **2019**, *116* (6), 1974–1983.

- (28) Dinega, D. P.; Bawendi, M. G. A Solution-Phase Chemical Approach to a New Crystal Structure of Cobalt. *Angew. Chem., Int. Ed.* **1999**, 38 (12), 1788–1791.
- (29) Kusada, K.; Kobayashi, H.; Yamamoto, T.; Matsumura, S.; Sumi, N.; Sato, K.; Nagaoka, K.; Kubota, Y.; Kitagawa, H. Discovery of Face-Centered-Cubic Ruthenium Nanoparticles: Facile Size-Controlled Synthesis Using the Chemical Reduction Method. *J. Am. Chem. Soc.* **2013**, *135* (15), 5493–5496.
- (30) Wang, C.; Chen, D. P.; Sang, X.; Unocic, R. R.; Skrabalak, S. E. Size-Dependent Disorder—Order Transformation in the Synthesis of Monodisperse Intermetallic PdCu Nanocatalysts. *ACS Nano* **2016**, *10* (6), 6345–6353.
- (31) Essinger-Hileman, E. R.; DeCicco, D.; Bondi, J. F.; Schaak, R. E. Aqueous room-temperature synthesis of Au–Rh, Au–Pt, Pt–Rh, and Pd–Rh alloy nanoparticles: fully tunable compositions within the miscibility gaps. *J. Mater. Chem.* **2011**, *21* (31), 11599–11604.
- (32) Marbella, L. E.; Andolina, C. M.; Smith, A. M.; Hartmann, M. J.; Dewar, A. C.; Johnston, K. A.; Daly, O. H.; Millstone, J. E. Gold-Cobalt Nanoparticle Alloys Exhibiting Tunable Compositions, Near-Infrared Emission, and High T2 Relaxivity. *Adv. Funct. Mater.* **2014**, 24 (41), 6532–6539.
- (33) Rodrigues da Silva, M.; Ângelo, A. C. D. Synthesis and Characterization of Ordered Intermetallic Nanostructured PtSn/C and PtSb/C and Evaluation as Electrodes for Alcohol Oxidation. *Electrocatalysis* **2010**, *1* (2), 95–103.
- (34) Kang, Y.; Pyo, J. B.; Ye, X.; Gordon, T. R.; Murray, C. B. Synthesis, Shape Control, and Methanol Electro-oxidation Properties of Pt–Zn Alloy and Pt3Zn Intermetallic Nanocrystals. *ACS Nano* **2012**, *6* (6), 5642–5647.
- (35) Liao, H.; Zhu, J.; Hou, Y. Synthesis and electrocatalytic properties of PtBi nanoplatelets and PdBi nanowires. *Nanoscale* **2014**, 6 (2), 1049–1055.
- (36) Zangari, G. Electrodeposition of Alloys and Compounds in the Era of Microelectronics and Energy Conversion Technology. *Coatings* **2015**, *5* (2), 195–218.
- (37) Sarah, N.; Schubert, K. Kristallstruktur von Pd5Bi2. J. Less-Common Met. 1979, 63 (2), P75-P82.
- (38) Asset, T.; Job, N.; Busby, Y.; Crisci, A.; Martin, V.; Stergiopoulos, V.; Bonnaud, C.; Serov, A.; Atanassov, P.; Chattot, R.; Dubau, L.; Maillard, F. Porous Hollow PtNi/C Electrocatalysts: Carbon Support Considerations To Meet Performance and Stability Requirements. *ACS Catal.* **2018**, *8*, 893–903.
- (39) Huang, X.; Shumski, A. J.; Zhang, X.; Li, C. W. Systematic Control of Redox Properties and Oxygen Reduction Reactivity through Colloidal Ligand-Exchange Deposition of Pd on Au. *J. Am. Chem. Soc.* **2018**, *140* (28), 8918–8923.
- (40) Du, B.; Tong. A Coverage-Dependent Study of Pt Spontaneously Deposited onto Au and Ru Surfaces: Direct Experimental Evidence of the Ensemble Effect for Methanol Electro-Oxidation on Pt. J. Phys. Chem. B 2005, 109 (38), 17775—17780.
- (41) Masa, J.; Batchelor-McAuley, C.; Schuhmann, W.; Compton, R. G. Koutecky-Levich analysis applied to nanoparticle modified rotating disk electrodes: Electrocatalysis or misinterpretation. *Nano Res.* **2014**, 7 (1), 71–78.
- (42) Lee, J.-M.; West, A. C. Impact of Pulse Parameters on Current Distribution in High Aspect Ratio Vias and Through-Holes. *J. Electrochem. Soc.* **2005**, *152* (10), C645.